Kovove Mater. 64 2026 95–105
DOI: 10.31577/km.2026.2.95

Microstructure and properties of graphene/AlCoCrNiMo$_x$ high-entropy alloy composites

Xingwu Qiu[1]*

[1]*Sichuan University of Architectural Technology, Deyang 618000, P. R. China*

Received 3 May 2026, received in revised form 19 May 2026, accepted 2 June 2026

Abstract

To address the insufficient strength-toughness, wear resistance, and corrosion resistance of AlCoCrNiMo$_x$ high-entropy alloys, graphene (Gr)-reinforced AlCoCrNiMo$_x$ (x = 0.1, 0.2, 0.3, 0.4) high-entropy alloy composites were fabricated by vacuum arc melting. The regulatory mechanisms of Mo content and graphene on the phase composition, microstructure, and comprehensive properties of the alloys were systematically revealed primarily via qualitative analysis, without quantitative separation of individual strengthening contributions. The phase structure, morphology, and elemental distribution were characterized using X-ray diffraction (XRD), scanning electron microscopy (SEM), and energy-dispersive X-ray spectroscopy (EDS). Microhardness, dry sliding wear behavior, and electrochemical corrosion performance in 3.5 wt.% NaCl solution were tested. The results show that the as-cast microstructure of the composite consists of an FCC phase, a B2 ordered phase, and a minor σ phase. With increasing Mo content from 0.1 to 0.4, the fraction of the FCC phase gradually decreases, while those of the B2 and σ phases continuously increase; the grains transform from coarse equiaxed grains to fine columnar grains. Graphene is inferred to be uniformly distributed at grain boundaries and phase boundaries, which is proposed to significantly refine grains, suppress elemental segregation, and forms a sound interfacial bond with the matrix. Mechanical and corrosion tests indicate that the hardness and wear resistance of the alloy increase continuously with increasing Mo content. The composite exhibits optimal comprehensive performance at x = 0.4 with 0.5 wt.% graphene addition: a microhardness of 625 HV, a wear rate as low as 2.75 × 10^{-6} mm^3 N^{-1} m^{-1}, and a corrosion current density of 3.82 × 10^{-6} A cm^{-2}. The synergistic improvement in comprehensive properties is attributed to the combined effects of solid-solution strengthening by Mo, second-phase strengthening by B2 and σ phases, as well as grain refinement, dispersion strengthening, self-lubrication, and physical barrier effects of graphene. This study focuses on qualitative discussion of the synergistic mechanisms, and the individual contribution of each mechanism is not quantified separately. This study provides experimental evidence and theoretical support for the compositional design and engineering applications of high-performance high-entropy alloy composites.

K e y w o r d s: high-entropy alloy, AlCoCrNiMo$_x$, graphene, microstructure, mechanical property, corrosion resistance

1. Introduction

High-entropy alloys (HEAs) are a novel class of multi-principal element alloys that break through the design philosophy of conventional alloys [1–5], typically composed of five or more metallic elements in equiatomic [6–8] or near-equiatomic ratios [9–11]. HEAs possess high strength [12–14], high hardness, excellent wear resistance [15, 16], and corrosion resistance [17–20], showing broad application prospects in harsh service environments such as aerospace, marine engineering, and high-end equipment manufacturing. AlCoCrNiMo-based HEAs are typical dual-phase HEAs, in which Al promotes the formation of the Al-Ni enriched ordered B2 phase to enhance strength; Cr and Mo significantly improve corrosion and wear

*Corresponding author: e-mail address: qiuxingwu2026@163.com

resistance, whereas variation in Mo content induces the precipitation of brittle intermetallic compounds such as the σ phase, thereby tailoring the phase composition and property matching.

However, single $AlCoCrNiMo_x$ HEAs still suffer from distinct performance limitations: at low Mo contents, the alloys show good ductility but insufficient hardness and wear resistance; at high Mo contents, hardness increases but ductility decreases, and overall corrosion resistance hardly meets the requirements of aggressive marine environments. As a two-dimensional nanomaterial with ultrahigh strength (130 GPa), excellent thermal and electrical conductivity, and self-lubricating characteristics, graphene features weak interlayer van der Waals forces that facilitate interlayer sliding, rendering exceptional solid lubrication properties. It is an ideal reinforcement for improving the comprehensive performance of metal matrix composites. Incorporating graphene into HEA systems can potentially synergistically optimize strength-toughness, wear resistance, and corrosion resistance via grain refinement, segregation suppression, and interfacial bonding enhancement. Preliminary applications have been reported in CoCrFeNi and other HEAs, yet systematic studies on graphene-reinforced $AlCoCrNiMo_x$ (x = 0.1–0.4) HEAs remain scarce, especially regarding the synergistic regulatory mechanisms of Mo content and graphene on microstructure and properties.

Accordingly, graphene/$AlCoCrNiMo_x$ (x = 0.1–0.4) HEA composites were prepared by vacuum arc melting in this work. The phase structure and microstructure were characterized by XRD, SEM, and EDS. Hardness, wear resistance, and corrosion resistance were systematically tested to reveal the intrinsic mechanisms underlying microstructural evolution and property reinforcement regulated by Mo content and graphene, with emphasis on qualitative analysis rather than quantitative evaluation of individual mechanism contributions, and distinguishing between experimental observations and proposed mechanisms. The compositional design was optimized to provide experimental and theoretical support for developing high-performance HEA composites.

2. Experimental materials and methods

2.1. Experimental materials

High-purity metal powders of Al, Co, Cr, Ni, and Mo (purity $\geq$ 99.9%) were used as raw materials. The reinforcement was multi-layer graphene powder with a flake size of 5–10 μm, thickness of 1–3 nm, and purity $\geq$ 99.5 %. The alloy composition was designed as an atomic ratio of Al:Co:Cr:Ni = 1:1:1:1, with Mo atomic ratios x = 0.1, 0.2, 0.3, and 0.4. The graphene content was fixed at 0.5 wt.%, determined by preliminary experiments to ensure uniform dispersion without agglomeration-induced property degradation.

2.2. Alloy fabrication

Graphene/$AlCoCrNiMo_x$ HEA composites were prepared using a DHL-300 vacuum arc melting furnace, with the detailed procedure as follows.

2.2.1. Raw material pretreatment

Graphene powder was ultrasonically dispersed in anhydrous ethanol at 300 W for 30 min, followed by vacuum drying at 60 ℃ for 12 h to remove residual moisture and ethanol, preventing graphene agglomeration and oxidation during melting.

2.2.2. Powder mixing

Metal powders and pretreated graphene were weighed accurately according to the designed ratio and placed in an agate mortar. A small amount of anhydrous ethanol was added as a dispersant, followed by manual grinding for 30 min. The mixture was then transferred to a planetary ball mill with agate balls as grinding media, and wet ball milling was performed at a ball-to-powder ratio of 10 : 1 and a rotation speed of 300 r min^{-1} for 4 h to ensure inferred uniform graphene dispersion in the metal powders. The milled slurry was vacuum-dried at 60 ℃ for 12 h and sieved through a 200-mesh screen to obtain a uniformly mixed graphene/metal powder.

2.2.3. Vacuum arc melting

The mixed powder was loaded into a water-cooled copper crucible, and the furnace chamber was sealed. A mechanical pump and a molecular pump were used in combination to achieve a vacuum level of 5×10^{-3} Pa. High-purity argon (99.99% purity) was then introduced to −0.05 MPa as a protective atmosphere. The vacuum-argon flushing cycle was repeated three times to minimize oxygen and moisture contamination and prevent oxidation of Al, graphene, and other metals. Arc ignition was conducted using a 3 mm-diameter tungsten electrode with an arc current of 150–200 A and an arc temperature was no more than 3000 ℃ to fully melt the powder. Electromagnetic stirring (frequency 50 Hz) was applied to promote melt convection and elemental diffusion, suppressing chemical segregation. Each melting cycle lasted 5 min before cooling to room temperature; the ingot was flipped 180 ℃ and remelted five times to improve chemical homogeneity and reduce microsegregation. After the final melting cycle, the ingot was

furnace-cooled to room temperature (25 °C in the water-cooled copper crucible and demolded to obtain a disk-shaped ingot with a diameter of 30 mm and thickness of 5 mm.

2.2.4. Sample processing and pretreatment

Ingots were cut into 10 mm × 10 mm × 5 mm blocks for hardness, wear, and corrosion tests, and ø 10 mm × 2 mm disks for XRD analysis. All samples were gradually ground with 400#, 800#, 1200#, and 2000# SiC papers to remove surface oxides and machining marks, then mechanically polished to a mirror finish with 1.5 mm diamond paste. Finally, samples were ultrasonically cleaned in anhydrous ethanol for 15 min, dried with cold air, and stored in a vacuum drying cabinet.

2.3. Testing and characterization

X-ray diffraction (XRD) was performed on a DX-2600 diffractometer with Cu Kα radiation (λ = 0.15406 nm), scanning over $2\theta = 20°$–$100°$ at $2°$ min^{-1} with a step size of 0.02°, operating at 40 kV and 40 mA. Rietveld refinement was performed to assist phase identification, though detailed refinement quality indicators and quantitative phase fractions are not reported in this study. The effects of Mo content and graphene on phase composition were analyzed based on XRD patterns.

Microstructure, grain size, and graphene distribution were observed using a KYKY-EM3200 scanning electron microscope (SEM) equipped with a QUANTAX-100 energy-dispersive X-ray spectrometer (EDS) for point and mapping analysis to determine elemental distribution and segregation behavior. It should be noted that SEM-EDS has limited capability for direct and definitive characterization of graphene in metallic matrices, and the uniform distribution of graphene is inferred from microstructural and elemental distribution features.

Microhardness was measured using an MHVS1000Z Vickers hardness tester under a 500 g load with a 15 s dwell time. Five separate positions were tested per sample; the average value after excluding the maximum and minimum was taken as the microhardness.

Wear performance was evaluated on an HT-1000 friction-wear tester under dry sliding conditions, with a GCr15 steel ball (6 mm diameter, 62 HRC) as the counterpart. Testing parameters: 5 N load, 0.2 m s^{-1} sliding speed, 30 min duration, and 360 m sliding distance. Wear morphologies were observed using the KYKY-EM3200 SEM.

Corrosion resistance in simulated seawater (3.5 wt.% NaCl solution) at 25 °C was assessed via potentiodynamic and cyclic polarization curves using a CS310M electrochemical workstation. A three-electrode system was employed: the alloy sample (exposed area 1 cm^2, non-working surfaces sealed with epoxy resin) as the working electrode, a saturated calomel electrode (SCE) as the reference electrode, and a platinum sheet as the counter electrode.

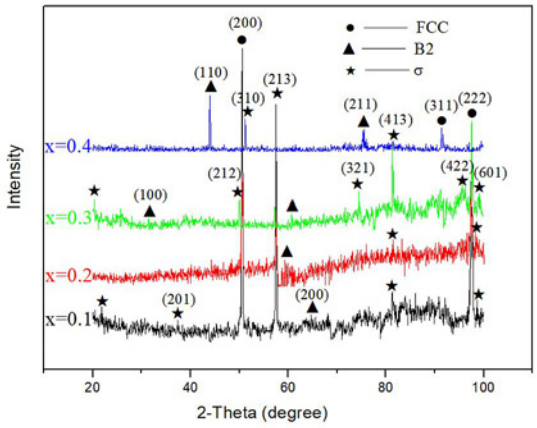

Fig. 1. XRD patterns of Gr/AlCoCrNiMo$_x$ alloys.

Potentiodynamic polarization curves were recorded from −1.2 to 1.5 V (vs SCE) at 1 mV s^{-1} after stabilizing the open-circuit potential for 30 min. Corrosion potential (E_{corr}) and corrosion current density (I_{corr}) were obtained by fitting.

3. Results and discussion

3.1. XRD

Figure 1 shows the XRD patterns of graphene/AlCoCrNiMo$_x$ (x = 0.1–0.4) composites. All samples consist of face-centered cubic (FCC) phase, ordered body-centered cubic B2 phase, and a small amount of σ topologically close-packed (TCP) phase, with distinct characteristic diffraction peaks and stable phase constitution.

The FCC phase, mainly composed of Co and Ni, shows strong diffraction peaks at $2\theta \approx 50.7°$, 96.5°, and 98°, acting as the ductile matrix. The intensity of FCC diffraction peaks gradually decreases with increasing Mo content, indicating a declining volume fraction. The B2 phase, formed by ordered Al-Ni bonding, exhibits characteristic peaks at $2\theta \approx 31.2°$, 44.8°, and 65.3°, serving as a high-strength reinforcing phase; elevated Mo content markedly enhances B2 peak intensity and promotes its precipitation and growth. σ phase diffraction peaks appear at $2\theta \approx$ 38.6°, 49.6°, 51°, and 57°, with slightly increased intensity at higher Mo content. This phase forms via Cr and Mo segregation at grain boundaries and acts as a hard, brittle wear-resistant phase. Owing to the low content (0.5 wt.%) and uniform dispersion of

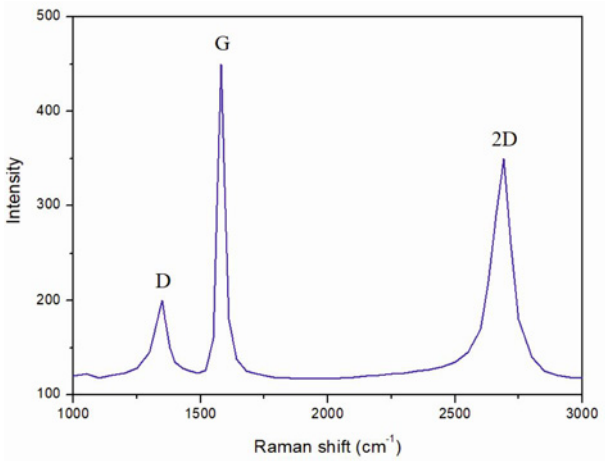

Fig. 2. Raman spectrum of Gr/AlCoCrNiMo$_{0.2}$ high-entropy alloy.

graphene, no obvious characteristic peak is observed at $2\theta \approx 26.5°$.

To verify the structural stability of graphene after arc melting and exclude the formation of brittle carbides (Cr_7C_3 and Mo_2C) at high temperature, room-temperature micro-Raman spectroscopy was performed on the Gr/AlCoCrNiMo$_{0.2}$ high-entropy alloy. The test was conducted using an excitation wavelength of 532 nm, a laser power of 2 mW, and a scanning range of 1000–3000 cm^{-1}. The corresponding Raman spectrum is displayed in Fig. 2. Obvious characteristic peaks located at 1352, 1585, and 2698 cm^{-1} were detected, corresponding to the D peak, G peak, and 2D peak of graphene, respectively. The sharp G peak indicates the intact sp conjugated carbon skeleton of graphene. The relatively weak D peak demonstrates minor structural defects after melting, and the symmetric single 2D peak confirms the retention of few-layer graphene structure. The calculated intensity ratio I_D/I_G was 0.44, which was considerably lower than the defect ratio (0.85–1.10) of graphene subjected to high-temperature oxidative degradation. This result indicates that the short-term high temperature during arc melting likely does not cause severe structural collapse of graphene under the present processing conditions. Meanwhile, no characteristic Raman peaks of Cr_7C_3 (650–720 cm^{-1}) and Mo_2C (810–890 cm^{-1}) were detected. Nevertheless, Raman analysis alone cannot fully rule out trace carbide formation or localized interfacial reactions, and graphene exhibits good structural stability within the alloy matrix under the tested conditions.

The Scherrer equation was utilized to calculate the full width at half maximum (FWHM) of XRD characteristic diffraction peaks, thereby obtaining the coherent scattering crystallite size inside the alloy. After graphene addition, the full width at half maximum (FWHM) of FCC and B2 diffraction peaks increases significantly, and grain size is refined from 80–120 nm to 40–70 nm, confirming that graphene acts as heterogeneous nucleation sites and exerts a pronounced grain-refining effect, consistent with SEM and EDS results.

Mo is a key element regulating phase constitution: it reduces the formation energy of the B2 phase and promotes Cr-Mo segregation at grain boundaries to trigger σ precipitation, realizing directional tailoring of FCC/B2/σ phase ratios. Graphene does not alter the intrinsic phase types but is proposed to refine grains via heterogeneous nucleation and optimize the microstructure, laying a foundation for subsequent property enhancement [20].

3.2. Microstructure and elemental distribution analysis

3.2.1. Microstructural evolution

Figure 3 shows the microstructures of graphene/AlCoCrNiMo$_x$ composites, clearly revealing grain morphology and evolution.

Gr/AlCoCrNiMo$_{0.1}$ is dominated by coarse equiaxed grains (5–15 μm), with FCC as the matrix and fine B2 particles dispersed; no obvious σ phase is observed, and graphene is uniformly distributed at grain boundaries as thin flakes. Gr/AlCoCrNiMo$_{0.2}$ shows significantly refined grains (3–10 μm), transforming from equiaxed to short columnar grains; the B2 phase increases and distributes discontinuously at grain boundaries, with a small amount of σ phase precipitated. Gr/AlCoCrNiMo$_{0.3}$ exhibits typical columnar grains, with B2 distributed in continuous bands and σ phase precipitated semi-continuously along grain boundaries, dividing the FCC phase. Gr/AlCoCrNiMo$_{0.4}$ possesses fine, uniform columnar grains (only 2–5 μm), with B2 forming a continuous network and σ phase wrapping grain boundaries in a complete network; graphene is uniformly distributed at grain and phase boundaries with sound interfacial bonding.

In Fig. 3, the grain sizes ranging from 2–15 μm observed by SEM correspond to macroscopic metallographic grains enclosed by high-angle grain boundaries. After solidification via vacuum arc melting, a single micrometer-scale macroscopic grain is internally composed of numerous nanoscale coherent crystallites, subgrains, and dislocation cells. SEM can only identify the overall grain profile outlined by high-angle grain boundaries, while it cannot distinguish the internal nanoscale subcrystalline domains. During melting and solidification, the graphene-reinforced AlCoCrNiMo high-entropy alloy exhibits obvious subcrystalline structures and lattice distortion.

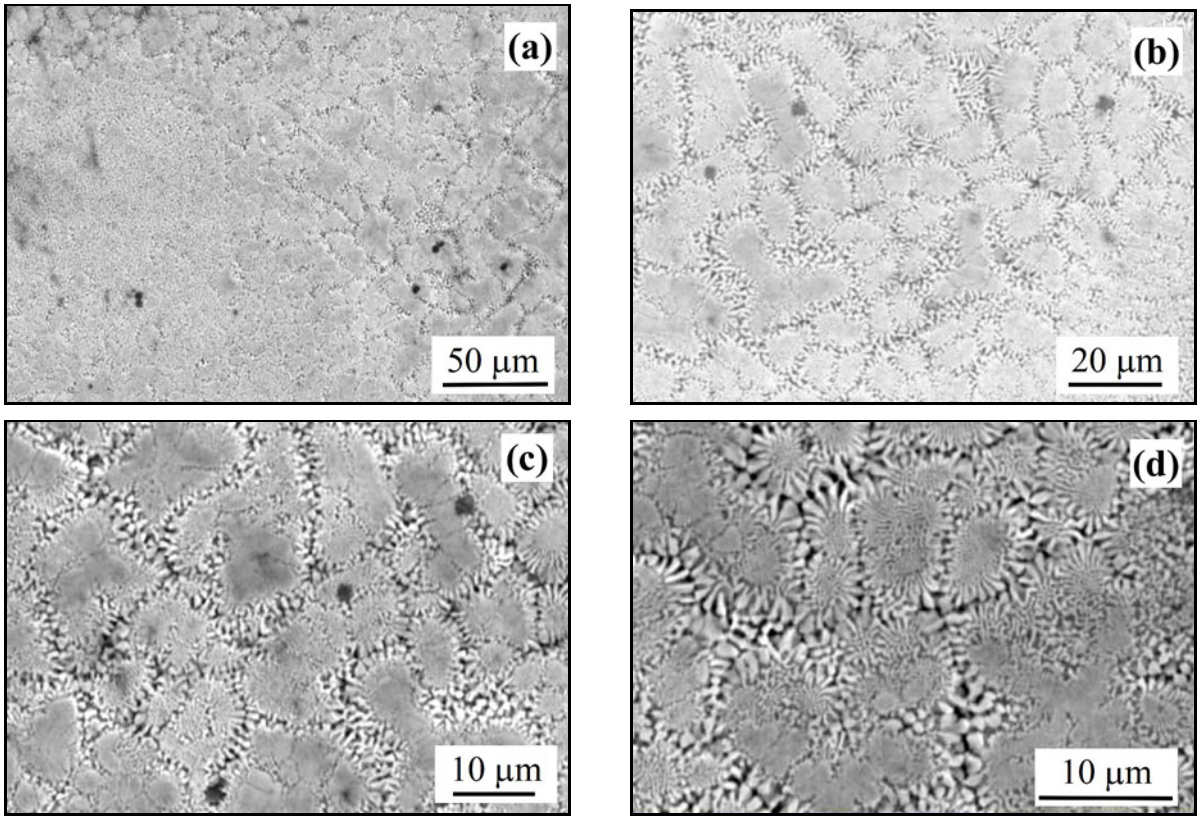

Fig. 3. Microstructure of Gr/AlCoCrNiMo$_x$ alloys: (a) Gr/AlCoCrNiMo$_{0.1}$, (b) Gr/AlCoCrNiMo$_{0.2}$, (c) Gr/AlCoCrNiMo$_{0.3}$, and (d) Gr/AlCoCrNiMo$_{0.4}$.

XRD characterizes the minimum ordered coherent lattice domains inside grains at the nanoscale, whereas SEM characterizes intact macroscopic grains defined by high-angle grain boundaries at the micrometer scale. These two scales are not contradictory and represent multi-scale characterization of different structural levels within the same microstructure. After graphene addition, the coherent crystallite size is refined from 80–120 nm to 40–70 nm, which reflects the refinement of internal subgrains and lattice domains rather than the variation of macroscopic grain size. This further confirms that graphene can induce lattice distortion and refine the internal subcrystalline structure of the alloy matrix.

With increasing Mo content, the microstructure evolves from coarse equiaxed grains to short columnar and then fine columnar grains; the FCC fraction decreases, while B2 and σ fractions increase continuously and form network structures. Graphene markedly refines grains, suppresses elemental segregation, and homogenizes and densifies the microstructure, consistent with XRD analysis.

Increasing Mo content alters the solidification path and growth rate, driving the equiaxed-to-columnar grain transition; B2 and σ phases precipitate along grain boundaries to form a skeleton, further restricting grain growth. With its high specific surface area, graphene adsorbs atoms, increases grain boundary density, and significantly weakens elemental segregation, leading to a more uniform and dense microstructure.

3.2.2. Elemental distribution characteristics

Figure 4 presents the EDS mapping of Gr/AlCoCrNiMo$_{0.4}$ composite. The elements show distinct regional enrichment: Al and Ni are mainly concentrated in the B2 phase; Co and Ni are distributed in the FCC matrix; Cr and Mo are significantly segregated in the σ phase and grain boundaries, owing to their nature as σ-forming elements and large atomic radii that favor grain boundary segregation.

After graphene addition, the distribution of Al, Co, Cr, Ni, and Mo becomes more uniform, and Cr-Mo segregation at grain boundaries is notably reduced. No obvious elemental diffusion layer is observed at the graphene-matrix interface, which is dominated by physical bonding without harmful reaction products.

Ordered Al-Ni pairing is essential for stabilizing the B2 phase, while Cr-Mo segregation directly accounts for σ nucleation and growth. Graphene is proposed to alleviate grain boundary segregation effectively by refining grains to shorten diffusion paths and adsorbing solute atoms. The interface is mainly

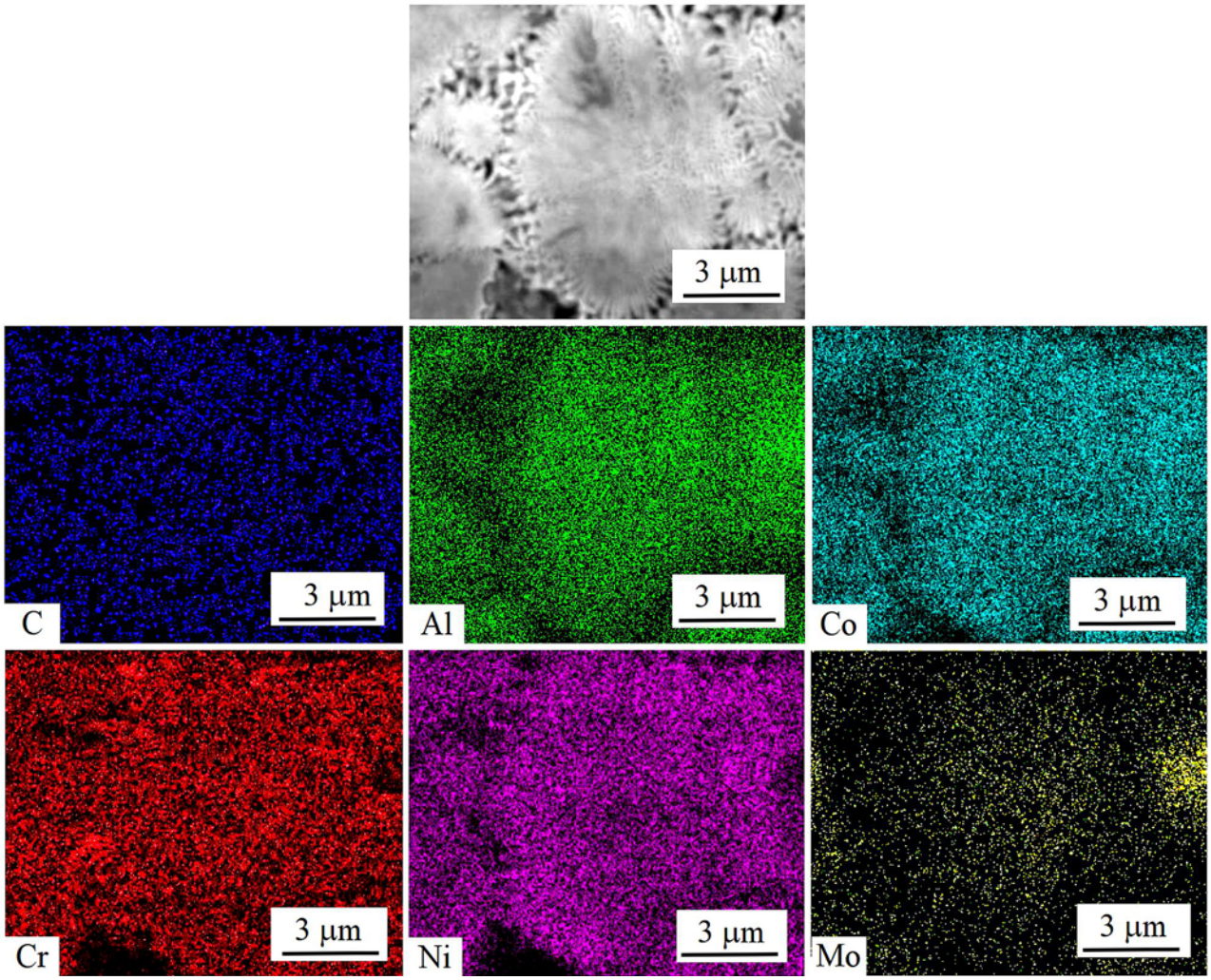

Fig. 4. EDS mapping of Gr/AlCoCrNiMo$_{0.4}$ alloy.

physical, avoiding brittle intermetallic formation that would degrade performance.

3.3. Mechanical properties

3.3.1. Microhardness

Figure 5 shows the microhardness of AlCoCrNiMo$_x$ (x = 0.1–0.4) alloys and Gr/AlCoCrNiMo$_x$ (x = 0.1–0.4) composites. It can be seen that the microhardness of alloys with different Mo contents is improved after the addition of graphene. The main strengthening mechanisms are summarized as follows: graphene acts as heterogeneous nucleation sites during solidification, which inhibits grain growth, refines the internal nanoscale coherent crystallites, increases grain boundary density, and hinders plastic deformation, thereby improving the hardness of the alloy. In addition, few-layer graphene is uniformly distributed inside grains and at grain boundaries. As a stable two-dimensional reinforcing phase, graphene breaks the continuous matrix structure, effectively restrains grain agglomeration and elemental segregation, and produces a prominent dispersion-strengthening effect.

The hardness increases continuously with Mo content, showing a clear positive correlation: 420 HV at x = 0.1, 485 HV at x = 0.2, 560 HV at x = 0.3, and 625 HV at x = 0.4.

The hardness enhancement arises from a synergistic combination of mechanisms:

Solid-solution strengthening: the atomic radius of Mo (0.139 nm) differs from those of matrix elements (Al: 0.143 nm, Co: 0.125 nm, Cr: 0.128 nm, Ni: 0.125 nm). Mo dissolved in FCC and B2 phases causes lattice distortion, hindering dislocation motion and increasing deformation resistance.

Second-phase strengthening: with increasing Mo content, the fractions of B2 ($\sim$ 500 HV) and σ ($\sim$ 1000 HV) increase; these hard, brittle phases effectively impede dislocation slip and significantly boost hardness.

Grain-refinement strengthening: graphene acts as

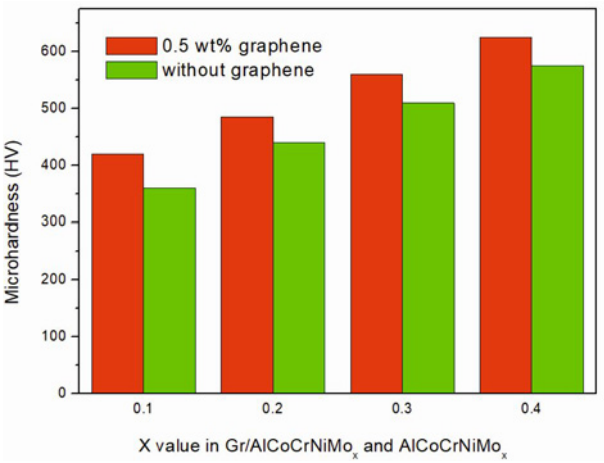

Fig. 5. Microhardness of AlCoCrNiMo$_x$ and Gr/AlCoCrNiMo$_x$ alloys.

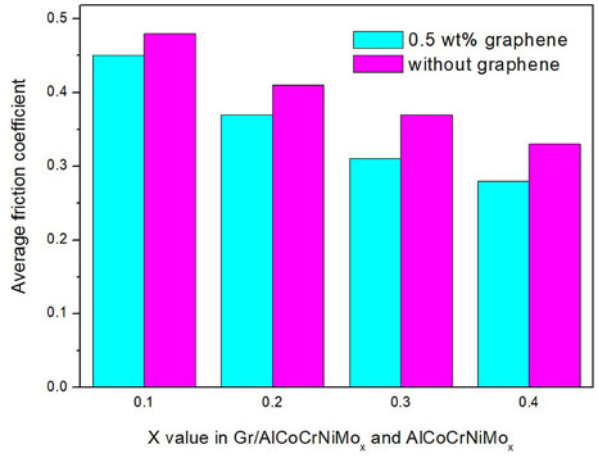

Fig. 6. Average friction coefficient of Gr/AlCoCrNiMo$_x$ alloys.

heterogeneous nucleation sites to refine grains; according to the Hall-Petch relationship, smaller grains correspond to higher hardness [21].

Dispersion strengthening: uniformly dispersed graphene in the matrix and at grain boundaries further hinders dislocation motion and enhances deformation resistance.

It should be emphasized that these strengthening mechanisms act synergistically, and their individual contributions cannot be quantitatively separated in the present study. These interpretations represent proposed mechanisms based on experimental observations, rather than directly verified conclusions.

3.3.2. *Wear resistance*

Figure 6 shows the average friction coefficient and Fig. 7 the wear rate of AlCoCrNiMo$_x$ alloys and Gr/AlCoCrNiMo$_x$ composites.

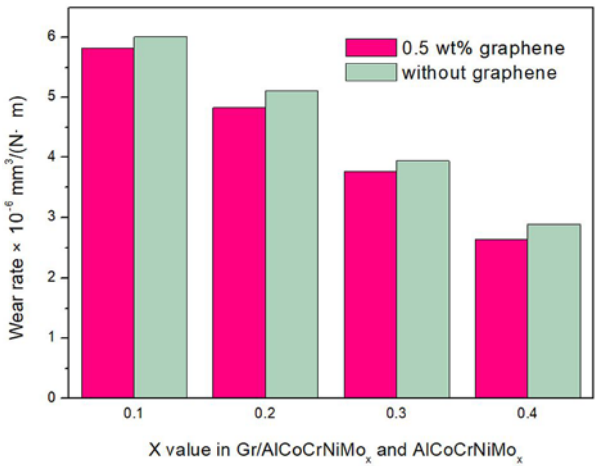

Fig. 7. Wear rate of Gr/AlCoCrNiMo$_x$ alloys.

With increasing Mo content, the friction coefficient decreases gradually and the wear rate continuously drops: the friction coefficient falls from 0.45 (x = 0.1) to 0.28 (x = 0.4); the wear rate decreases from 5.82×10^{-6} to 2.75×10^{-6} mm^3 N^{-1} m^{-1}. Weak van der Waals forces between graphene layers facilitate interlayer sliding during friction, which is proposed to form a continuous transferred lubricating film at the contact interface. This reduces frictional resistance between the alloy and the counterpart, mitigating abrasive and adhesive wear and markedly improving wear resistance.

Figure 8 displays the worn surface morphologies of graphene/AlCoCrNiMo$_x$ composites. At low Mo contents, the worn surfaces exhibit obvious ploughing grooves and spalling pits, with abrasive and adhesive wear as the dominant mechanisms. At high Mo contents, the surfaces become smoother, with shallower grooves and fewer pits; the wear mechanism transitions to mild abrasive and oxidative wear. Graphene is proposed to form a continuous transferred lubricating film, further lowering frictional resistance and material loss.

To directly verify the formation of graphene transfer lubricating film during friction, micro-area Raman tests were performed on the wear tracks of the Gr/AlCoCrNiMo$_{0.3}$ alloy after wear experiments. The corresponding test results are presented in Fig. 9. Clear D, G, and 2D characteristic peaks of graphene can still be observed on the worn alloy surface, indicating that no chemical reaction occurred between graphene and the metallic matrix during the friction process. After wear testing, the I_D/I_G ratio increased from 0.44 (as-cast state) to 0.53. This variation suggests that frictional shear force induced slight structural defects on the graphene nanosheets and simultaneously promoted the exfoliation and spreading of

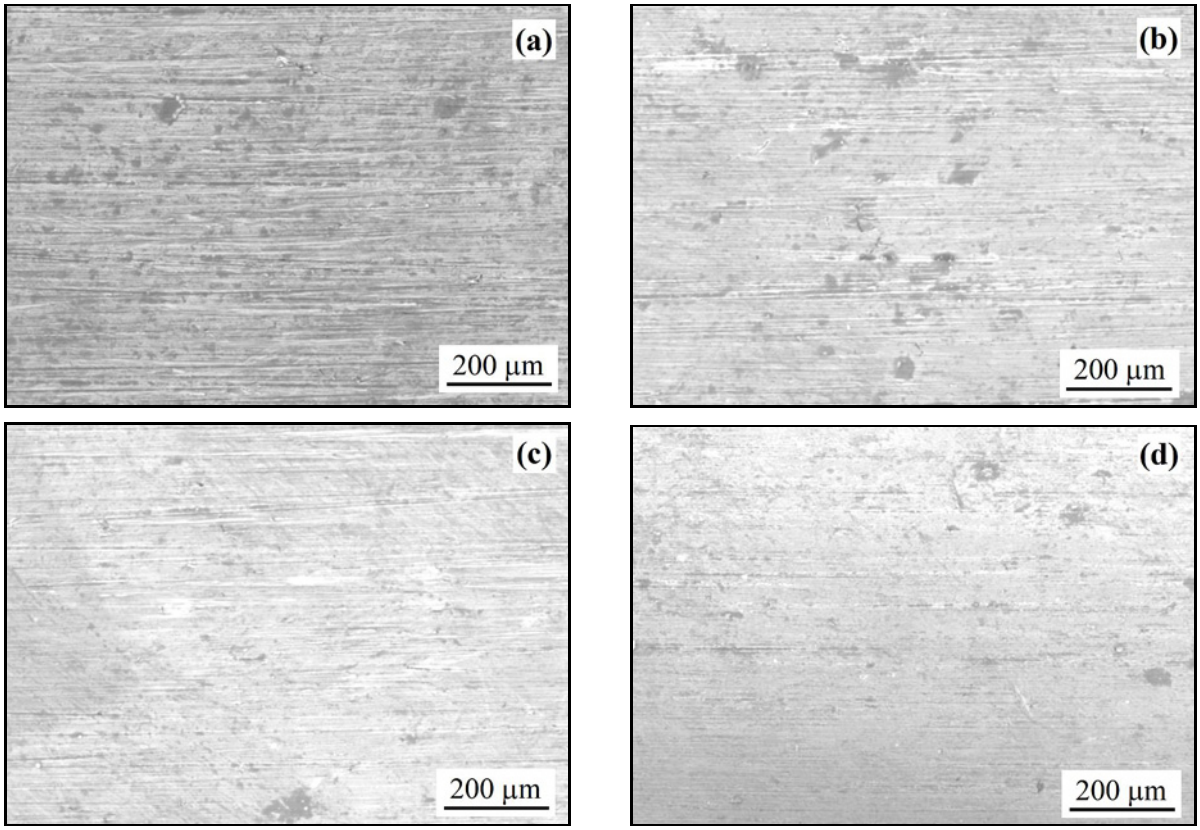

Fig. 8. Wear morphology of Gr/AlCoCrNiMo$_x$ alloys: (a) Gr/AlCoCrNiMo0.1, (b) Gr/AlCoCrNiMo0.2, (c) Gr/AlCoCrNiMo0.3, and (d) Gr/AlCoCrNiMo0.4.

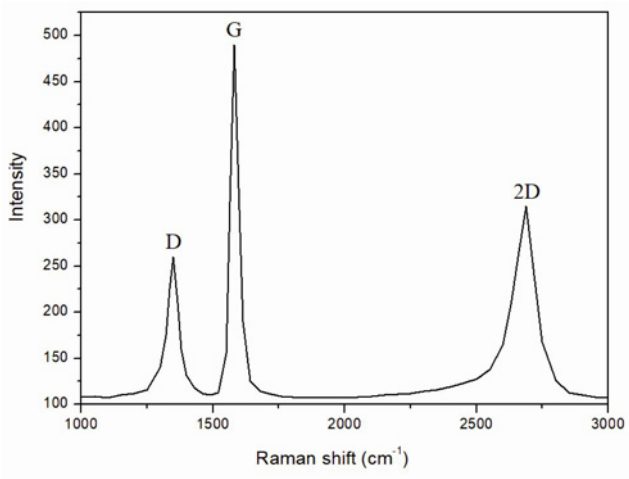

Fig. 9. Raman spectrum of Gr/AlCoCrNiMo$_{0.3}$ alloy after wear experiments.

graphene on the worn surface, thereby forming a continuous and dense carbon-based transfer film. Owing to the low interlayer shear resistance of graphene, the contact stress of the friction pair was effectively reduced, achieving excellent self-lubricating, friction-reducing and wear-resistant performances. Moreover, distinct D and G peaks were detected on the wear track without obvious peak shifting or miscellaneous oxidation peaks.

The exceptional self-lubricating property of graphene originates from facile interlayer sliding, which is proposed to form a protective lubricating film, reduces frictional resistance, and suppresses adhesive wear. At low Mo contents (x = 0.1–0.2), severe ploughing and spalling prevail, governed by abrasive + adhesive wear. With increasing Mo (x = 0.3–0.4), higher hardness flattens worn surfaces, reduces grooves and spalling, and shifts the mechanism to mild abrasive + oxidative wear; a dense oxide film (mainly Cr_2O_3, MoO_3) forms to protect the matrix. Graphene further smoothens worn surfaces, reduces ploughing, and resists abrasive embedding and matrix spalling, consistent with strengthening mechanisms reported for graphene-reinforced HEAs.

3.4. Corrosion resistance analysis

Figure 10 presents the potentiodynamic polarization curves of graphene/AlCoCrNiMo$_x$ composites in 3.5 wt.% NaCl solution. Table 1 lists the fitted E_{corr} and I_{corr}. I_{corr} is the core indicator for corrosion resistance: a smaller I_{corr} indicates a lower corrosion rate and better resistance; a more positive E_{corr} implies higher resistance to corrosion initiation.

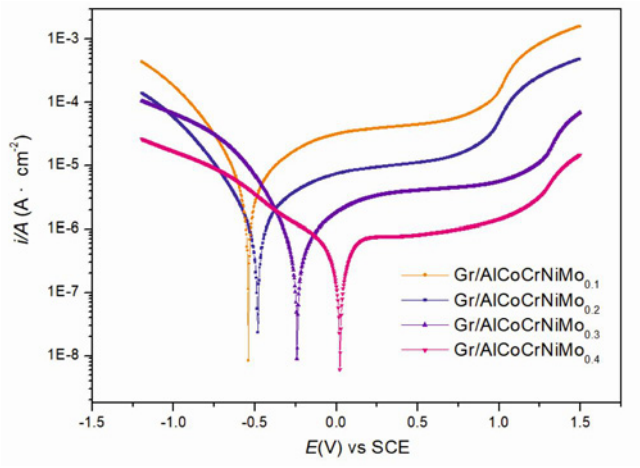

Fig. 10. Polarization curves of Gr/AlCoCrNiMo$_x$ in 3.5% NaCl solution.

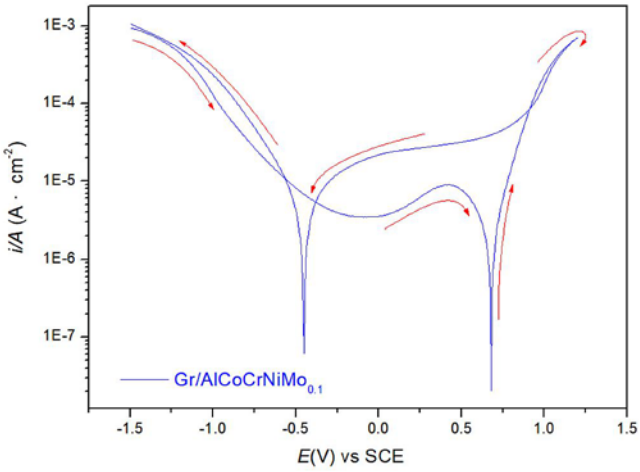

Fig. 11. Cyclic polarization curve of Gr/AlCoCrNiMo$_{0.1}$ in 3.5% NaCl solution.

Table 1. Corrosion dynamics parameters of Gr/AlCoCrNiMo$_x$ in 3.5% NaCl solution

Alloys	E_{corr} (V)	I_{corr} (A cm^{-2})
Gr/AlCoCrNiMo$_{0.1}$	–0.55	3.16×10^{-5}
Gr/AlCoCrNiMo$_{0.2}$	–0.48	6.76×10^{-6}
Gr/AlCoCrNiMo$_{0.3}$	–0.24	4.52×10^{-6}
Gr/AlCoCrNiMo$_{0.4}$	0.05	3.82×10^{-6}

With increasing Mo from 0.1 to 0.4, E_{corr} shifts positively and I_{corr} decreases gradually, indicating continuously improved corrosion resistance: at $x = 0.1$, $E_{corr} = -0.55$ V (vs SCE) and $I_{corr} = 3.16 \times 10^{-5}$ A cm^{-2}; at $x = 0.4$, $E_{corr} = 0.05$ V (vs SCE), and $I_{corr} = 3.82 \times 10^{-6}$ A cm^{-2}. Mo promotes the formation of a dense Cr-Mo-rich passive film that effectively blocks C? penetration and suppresses anodic dissolution, consistent with reported mechanisms for Mo-modified HEAs. Graphene is proposed to provide an excellent physical barrier covering the surface, preventing contact between corrosive media (Cl^-, H_2O, O_2) and the matrix and reducing corrosion reactions. Meanwhile, grain refinement increases nucleation sites for a more continuous and stable passive film. Furthermore, the high electrical conductivity of graphene is proposed to disperse corrosion current and mitigate localized corrosion, enhancing corrosion stability.

Figure 11 shows the cyclic polarization curve of Gr/AlCoCrNiMo$_{0.1}$ in 3.5 wt.% NaCl solution. A negative hysteresis loop forms, indicating superior pitting corrosion resistance and a stable passive film resistant to localized breakdown under Cl^- attack.

Figure 12 displays the corroded surface morphology and elemental mapping of Gr/AlCoCrNiMo$_{0.4}$ composite. The surface is uniform without obvious pitting pits.

Mo facilitates the formation of a dense Cr-Mo-rich passive film that efficiently blocks Cl^- penetration and inhibits anodic dissolution [22]. Graphene is proposed to act as a two-dimensional physical barrier to isolate the matrix from corrosive media; grain refinement promotes a more continuous and stable passive film; and high conductivity is proposed to disperse corrosion current to prevent pit propagation.

4. Conclusions

Graphene/AlCoCrNiMo$_x$ ($x = 0.1$–0.4) HEA composites were successfully fabricated by vacuum arc melting. Graphene is inferred to be uniformly dispersed and bonds well with the matrix, without obvious agglomeration or harmful interfacial reactions.

The composites consist of FCC solid-solution phase, B2 ordered phase, and minor σ phase. With increasing Mo content, the FCC fraction decreases while B2 and σ fractions increase; the microstructure transforms from coarse equiaxed grains to fine columnar grains. Graphene does not change the phase constitution but is proposed to significantly refine grains and suppress elemental segregation.

Microhardness, wear resistance, and corrosion resistance increase continuously with Mo content and are further enhanced by graphene. The composite achieves optimal comprehensive performance at $x = 0.4$ with 0.5 wt.% graphene: 625 HV, 2.75×10^{-6} mm^3 N^{-1} m^{-1}, and 3.82×10^{-6} A cm^{-2}.

The core strengthening mechanisms include solid-solution strengthening by Mo, second-phase strengthening by B2 and σ phases, coupled with grain refinement, dispersion strengthening, self-lubrication, and

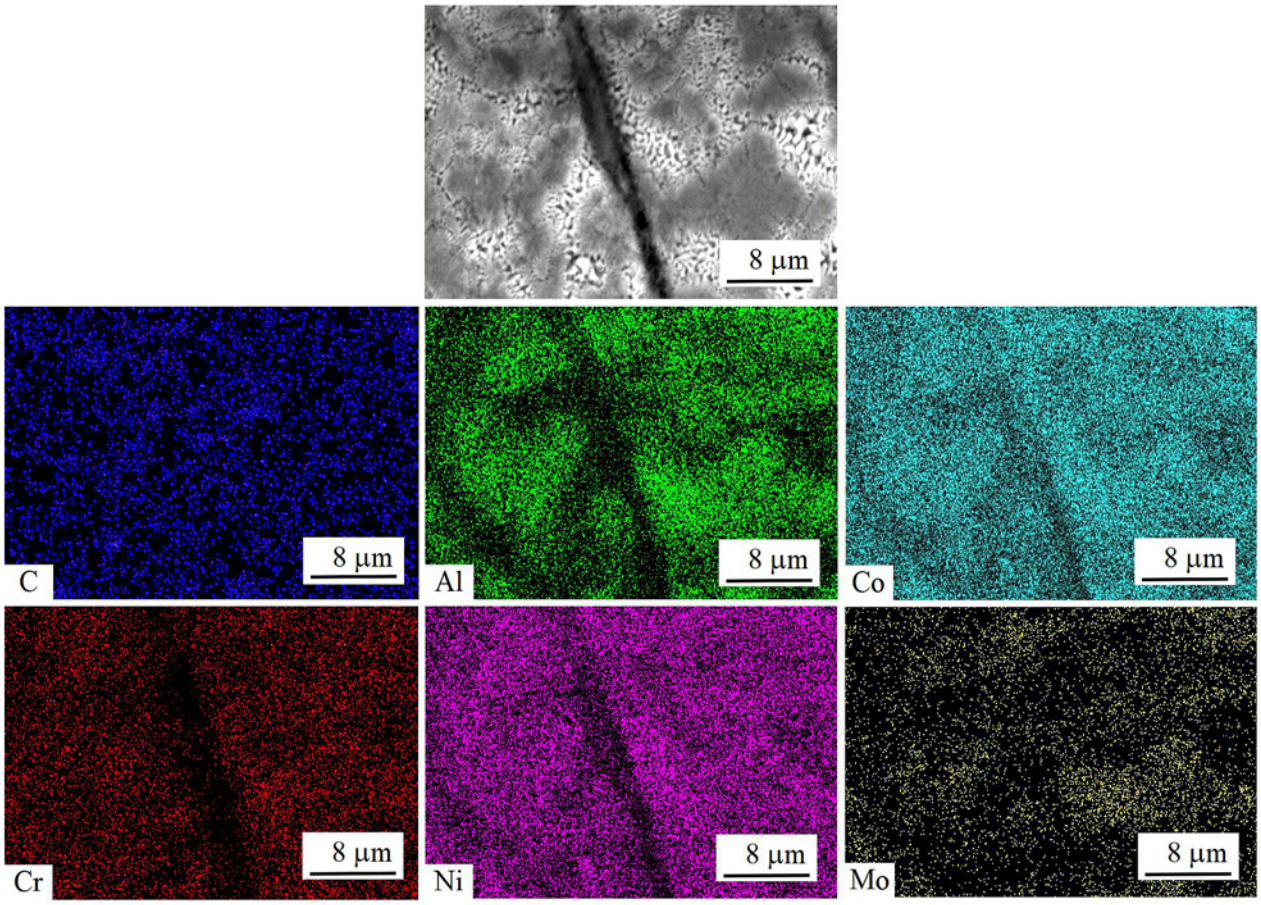

Fig. 12. Corrosion morphology and elemental mapping.

physical barrier effects of graphene. These mechanisms act synergistically, and their individual contributions are discussed qualitatively rather than quantified in this study. Mechanistic interpretations regarding graphene effects represent proposed explanations based on experimental evidence, not fully verified conclusions.

Graphene/AlCoCrNiMo$_{0.4}$ composite integrates high hardness, excellent wear resistance, and corrosion resistance with uniform microstructure and stable properties, providing an important reference for developing high-performance HEA composites for harsh marine and high-end equipment applications.

Acknowledgements

This work was supported by Multicomponent Alloys Key Laboratory of Deyang City, Sichuan College of Architectural Technology (2025MAKF02, 2025MAKF03, 2025MAKF04).

References

[1] J. W. Yeh, S. K. Chen, S. J. Lin, J. Y. Gan, T. S. Chin, T. T. Shun, C. H. Tsau, S. Y. Chang, Nanostructured high-entropy alloyswith multiple principal elements: Novel alloy design concepts and outcomes, Adv. Eng. Mater. 6 (2004) 299–303. https://doi.org/10.1002/adem.200300567

[2] S. W. Li, J. L. Li, J. M. Shi, Y. J. Du, Y. Peng, F. Jin, J. T. Xiong, F. S. Zhang, Microstructure and mechanical properties of the brazed region in the AlCoCrFeNi high-entropy alloy and FGH98 superalloy joint, Mater. Sci. Eng. A 804 (2021) 140714. https://doi.org/10.1016/j.msea.2020.140714

[3] C. G. Liu, X. W. Qiu, Z. S. Wang, B. Zhong, J. Peng, Z. W. Liu, H. Liu, Y. Gao, H. Q. Wu, X. Zhou, C. Q. Luo, X. R. Xie, C. Meng, Laser additive manufacturing of graphene/CoCrFeNiNbx coatings and their application in automatic measurement robot devices, Kovove Mater. 63 (2025) 271–277. https://doi.org/10.31577/km.2025.5-6.271

[4] X. W Qiu, C. G. Liu, J. Peng, Z. S. Wang, Corrosion behavior of CoCrNiAl high entropy alloy and other typical metals in simulated acid rain solution, Kovove Mater. 61 (2023) 59–67. https://doi.org/10.31577/km.2023.1.59

[5] T. Sonar, M. Ivanov, E. Trofimov, A. Tingaev, I. Suleymanova, An overview of microstructure, mechanical properties and processing of high entropy alloys and its future perspectives in aeroengine applications, Mater. Sci. Energy Technol. 7 (2024) 35–60. https://doi.org/10.1016/j.mset.2023.07.004
[6] M. Mirzaei, F. Habibi, G. Lee, S. S. Sohn, Microstructural evolution and mechanical properties of CoCrFeMnNi cantor high-entropy alloy severely deformed by the accumulative roll bonding (ARB) process, J. Mater. Res. Technol. 39 (2025) 4950–4962. https://doi.org/10.1016/j.jmrt.2025.10.190
[7] F. S. Tan, L. Li, J. Li, B. Liu, P. K. Liaw, Q. H. Fang, Multiscale modelling of irradiation damage behavior in high entropy alloys, Adv. Powder Mater. 2 (2023) 100114. https://doi.org/10.1016/j. apmate.2023.100114
[8] O. N. Senkov, G. B. Wilks, D. B. Miracle, C. P. Chuang, P. K. Liaw, Refractory high-entropy alloys, Intermetallics 18 (2010) 1758–1765. https://doi.org/10.1016/j.intermet.2010.05.014
[9] Y. J. Zhou, Y. Zhang, T. N. Kim, G. L. Chen, Microstructure characterizations and strengthening mechanism of multi-principal component AlCoCrFe $NiTi_{0.5}$ solid solution alloy with excellent mechanical properties, Mater. Lett. 62 (2008) 2673–2676. https://doi.org/10.1016/j.matlet.2008.01.011
[10] W. Li, W. Wang, M. C. Niu, K. Yang, J. H. Luan, H. W. Zhang, Z. B. Jiao, Unraveling the two-stage precipitation mechanism in a hierarchical-structured fcc/L21 high-entropy alloy: Experiments and analytical modeling, Acta Mater. 262 (2024) 119426. https://doi.org/10.1016/j.actamat.2023.119426
[11] M. Pozuelo, J. Marian, Microscale deformation controlled by compositional fluctuations in equiatomic Nb–Mo–Ta–W alloys, Mater. Sci. Eng. A 856 (2022) 143892. https://doi.org/10.1016/j.msea.2022.143892
[12] W. R. Wang, W. L. Wang, S. C. Wang, Y. C. Tsai, C. H. Lai, J. W. Yeh, Effects of Al addition on the microstructure and mechanical property of Al_xCoCrFeNi high-entropy alloys, Intermetallics 26 (2012) 44–51. https://doi.org/10.1016/j.intermet.2012.03.005
[13] T. F. Yang, S. Q. Xia, S. Liu, C. X. Wang, S. S. Liu, Y. Zhang, J. M. Xue, S. Yan, Y. G. Wang, Effects of AL addition on microstructure and mechanical properties of Al_xCoCrFeNi high-entropy alloy, Mater. Sci. Eng. A 648 (2015) 15–22. https://doi.org/10.1016/j.msea.2015.09.034
[14] K. Yue, L. Wang, Z. Xu, C. L. Cheng, Y. Q. Wang, Y. Fan, J. Xu, Z. J. Wang, Z. Chen, Effect of WC content on the microstructure and wear resistance of laser cladding AlCoCrFeNi$Ti_{0.5}$ high-entropy alloy coatings, Ceram. Int. 50 (2024) 41515–41526. https://doi.org/10.1016/j.ceramint.2024.08.001
[15] W. X. Fan, G. Q. Zhu, B. T. Jiang, B. X. Su, X. D. Liu, C. Liu, X. Liu, H. Guo, L. Wang, E. Bakhtiyor, L. S. Luo, Y. Q. Su, J. J. Guo, A dual-phase refractory high-entropy alloy with extremely high specific strength and excellent ultra-high temperature strength, Vacuum 246 (2026) 115072. https://doi.org/10.1016/j.vacuum.2026.115072
[16] A. A. Korda, D. P. T. Muhammad, F. Muhammad, T. L. Achmad, B. Prawara, D. H. Prajitno, B. H. Jihad, M. H. Setianto, E. A. Basuki, Microstructural stability and high temperature isothermal oxidation behavior studies of high entropy alloy Al0.5CoCrFeNi, Corros. Commun. 20 (2025) 100–115. https://doi.org/10.1016/j.corcom.2024.07.005
[17] A. Fu, B. Liu, Z. Z. Li, T. Yang, Y. K. Cao, J. He, B. Wang, J. Li, Q. Fang, X. Cheng, M. A. Meyers, Y. Liu, Superb impact resistance of nano-precipitation-strengthened high-entropy alloys, Adv. Powder Mater. 4 (2025) 100277. https://doi.org/10.1016/j.apmate.2025.100277
[18] L. X. Guo, S. W. Huang, W. Li, J. S. Lv, J. Sun, Theoretical design and experimental verification of high-entropy carbide ablative resistant coating, Adv. Powder Mater. 3 (2024) 100213. https://doi.org/10.1016/j.apmate.2024.100213
[19] H. B. Wang, L. Zhang, J. Deng, L. F. Li, Y. Rong, C. Tan, F. Wang, Microstructure and mechanical properties of ZrB_2 ceramic particle reinforced AlCoCrFeNi high entropy alloy composite materials prepared by spark plasma sintering, Ceram. Int. 50 (2024) 45311–45319. https://doi.org/10.1016/j.ceramint.2024.08.371
[20] S. L. Gong, Y. D. Wang, Y. C. Li, M. H. Song, Microstructure and properties of CoCrFeNiTi_x high-entropy alloy coating by laser cladding, Mater. Sci. Eng. Powder Metall. 29 (2024) 118–124. https://doi.org/10.19976/j.cnki.43-1448/TF.2024015
[21] Y. Dong, K. Y. Zhou, Y. P. Lu, X. X. Gao, T. M. Wang, T. J. Li, Effect of vanadium addition on the microstructure and properties of AlCoCrFeNi high entropy alloy, Mater. Design 57 (2014) 67–72. https://doi.org/10.1016/j.matdes.2013.12.048
[22] J. Fan, C. Chen, H. W. Yao, K. Xu, J. Liu, J. B. Pu, Corrosion and wear behaviors of AlCo$Cr_{1+x}Fe_{1-x}Ni_{2.1}$ high-entropy alloys, Corros. Commun. 20 (2025) 13–23. https://doi.org/10.1016/j.corcom.2024.07.009